Inorganic Chemistry Communications 140 (2022) 109424

Contents lists available at ScienceDirect

Inorganic Chemistry Communications

journal homepage: www.elsevier.com/locate/inoche

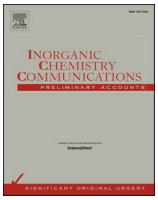

Short communication

ZIF-8 derived $CuFe_2O_4$ nanoparticles: Evolution of composition and microstructures, and their electrochemical performances as anode for lithium-ion batteries

A. Sankar [a], K. Paramasivaganesh [b,*], M. Parthibavarman [c], K.L. Meganathan [c]

[a] Department of Chemistry, Kandaswami Kandar's College, P. Velur, Namakkal 638182, Tamil Nadu, India
[b] Department of Chemistry, Arumugam Pillai Seethai Ammal College (APSAC), Thriupathur, Sivagangai 630211, Tamil Nadu, India
[c] PG and Research Department of Physics, Chikkaiah Naicker College, Erode 638004, Tamil Nadu, India

ARTICLE INFO

Keywords:
Metal organic framework
MOF derived $CuFe_2O_4$
Copper ferrite
Electrochemical performance
Li ion batteries

ABSTRACT

Improving electrical conductivity and exposing more active surface area in metal–organic frameworks remains a challenge. Metal-organic frameworks (MOF) are interesting precursor for developing new Li-ion battery electrode materials (LIBs). Herein, we report a convenient and straightforward one-pot hydrothermal strategy to prepare MOF-derived $CuFe_2O_4$. X-ray diffraction (XRD), Scanning electron microscope (SEM), Transmission electron microscope (TEM), and Brunauer-Emmett-Teller (BET) were used to evaluate the $CuFe_2O_4$ and $CuFe_2O_4$/ZIF-8 composites. $CuFe_2O_4$/ZIF-8 nanocomposites showed a noticeable improvement electrochemical property in terms of increased the discharge/charge capacity of $CuFe_2O_4$/ZIF-8 was determined to be 1478/980 $mAhg^{-1}$ as an anode for lithium ion batteries. Similarly the pure $CuFe_2O_4$ electrode exhibits discharge/charge was 986/678 $mAhg^{-1}$. The coulomb efficiency of $CuFe_2O_4$/ZIF-8 and $CuFe_2O_4$ was 70.8 and 91.3% respectively. In the end of 10th cycle, the discharge /charge capacity of $CuFe_2O_4$/ZIF-8 was found to be 790/695 $mAhg^{-1}$. Similarly the pure $CuFe_2O_4$ electrode exhibits discharge/charge was 560/535 $mAhg^{-1}$. Whereas, the columbic efficiency of $CuFe_2O_4$/ZIF-8 and $CuFe_2O_4$ was 79 and 69.5%, respectively (10th cycle). These outstanding electrochemical capabilities suggest that $CuFe_2O_4$ anode materials generated from MOFs (ZIF-8) could be used in high-performance Li-ion batteries.

1. Introduction

Batteries have an important role in the development of electrical energy utilization, such as in renewable energy and electric vehicles. Batteries with good performance would support the devices which utilized them. Because the amount of energy stored in a battery is limited, so battery getting charging and discharging cycles. Improper charge and discharge process could decrease the battery's performance. Therefore battery management system (BMS) is very necessary so that could maintain performance of the battery at optimum condition. Lithium-ion batteries have been employed in practically every automotive and commercial device since their invention. Electric vehicles have been viewed as a key aspect of ongoing attempts to cut greenhouse gas emissions in recent years. With the introduction of household electric vehicles, the demand for lithium-ion batteries with high energy and power density has increased. Graphite has been the most extensively utilized anode material to date. Its low specific capacity (372 mAhg-1) and lithium coating at fast charging rates, on the other hand, cause capacity loss and internal short-circuiting, as well as thermal explosion. Other resources are needed to address the existing challenges. Anodes made of alloys and transition metal oxides are popular possibilities. Alloy anodes, which have a larger capacity and are prevalent in the earth's crust, could be a viable option. Because of its high energy density, extended cycle life, and enormous rate capability, lithium ion batteries are widely utilized in power grids, electric cars, and consumer devices [1–4]. Traditional graphite anodes, on the other hand, have a low specific capacitance (372 $mAhg^{-1}$) and a rapid capacity decline, which limits their use in high-performance lithium ion batteries [5,6]. New anode materials with increased capacity and stability should be developed as a result. As a new form of anode material, mixed transitional metal oxides (MTMOs) with two metallic ions have gotten a lot of attention. They have a greater capacity factor than graphite anodes attributed to the beneficial effects of several metals [7,8].

Spinel metal ferrites have been presented as potential graphite anode

* Corresponding author.

https://doi.org/10.1016/j.inoche.2022.109424
Received 20 December 2021; Received in revised form 5 March 2022; Accepted 23 March 2022
Available online 26 March 2022

replacements. The creation and degradation of lithium oxide (Li_2O), as well as the reduction and oxidation of metal nanoparticles, are involved in the charge and discharge catalytic reaction in these compounds, which differs from traditional Li-ion insertion/extraction. $CuFe_2O_4$ (CFO) is one of these materials that have piqued researchers' interest due to its high theoretical capacity (895 $mAhg^{-1}$), low toxicity, and abundance in nature. $CuFe_2O_4$, on the other hand, has low conductivity, which is critical for better Li-ion batteries. Many researchers have concentrated on distributing $CuFe_2O_4$ on carbon matrices to produce composites to solve this issue [9]. MOFs are crystalline porous materials with geometries that link inorganic metal ions to organic linkers by stronger chemical bonds, and have sparked interest in a range of applications, including delivery of drugs, gas sorption, optoelectronics, catalyst supports, and energy storage [10–12]. Specific application, the structure of MOF materials can be altered by altering the metal core and organic units. Recently, MOFs have been used as sacrificial frameworks for the thermal or chemical production of various nanomaterials (porous carbon and metal oxides) [13–17]. Particularly, ZIF-8 framework (Zn (MeIM)2, MeIM = 2-methylimidazole) holds an intersecting 3D structure, high thermal and chemical stabilities, and large pore size and surface area, which are desirable for depositing metal NPs [18–22]. In this report, a simple aqueous suspension based hydrothermal reaction technique has been employed to fabricate uniform and well-adhered $CuFe_2O_4$/ZIF-8 metal organic frame work anode materials were prepared and used electro chemical performance based Li ion batteries. $CuFe_2O_4$/ZIF-8 composite electrodes with a wide surface area, high conductivity, and pore structure can efficiently bear the massive volumetric stresses created during lithiation/demonstrate outstanding cycle stability and rate capability.

2. Experimental section

2.1. Materials

Zinc nitrate hexahydrate ($Zn(NO_3)_2{\cdot}6H_2O$, 99% purity), copper nitrate hexahydrate ($Cu(NO_3)_2{\cdot}6H_2O$, 99% purity), iron nitrate hexahydrate ($Fe(NO_3)_2{\cdot}6H_2O$, 99% purity), 2-methylimidazole (Hmim, 99% purity) and ammonium hydroxide (NH4OH) were purchased from Sigma-Aldrich. In addition, deionized water was used as a solvent in the synthesis of ZIF-8. All these chemicals were used as received without any further purification.

2.2. Synthesis of ZIF-8

First, 0.25 g of zinc nitrate hexahydrate was added to 10 ml of deionized water and stirred for 10 min, 4.5 g of 2-methylimidazole was added to 70 ml of deionized water and stirred for 20 min. Thereafter, a mixed solution of zinc nitrate and 2-methylimidazole solution was stirred for 4 min, and the mixed solution was transferred to Teflon-lined autoclaves for hydrothermal synthesis at 120 °C for 8 h. the product was collected by centrifugation, washed several times with water and methanol, and vacuum-dried over-night at 70 °C.

2.3. Synthesis of $CuFe_2O_4$

Typically, 0.005 mol $Cu(NO_3)_2{\cdot}6H_2O$ and 0.010 mol $Fe(NO_3)_3{\cdot}6H_2O$ were dissolved together in 40 ml deionized water to form solution under magnetic stirring until the reactants were completely dissolved. The solution was adjusted the pH to 10 adding of 1 M NH_4OH drop wise and loaded into a 75 ml capacity Teflon lined vessel. The vessel was tightly closed and transferred to autoclave. The final solution was transferred to a 75 ml teflon-line stainless steel autoclave. The sealed autoclave was allowed to maintain at 180 °C for 12 h, then cooled down to ambient temperature. The final products were washed repeatedly with distilled water and absolute ethanol several times and then dried at 60 °C. Later, these powders were sintered at 500 °C at a heating rate of 5 °C/min for 5 h in an air atmosphere. The final product was labeled as pristine $CuFe_2O_4$ (brown color).

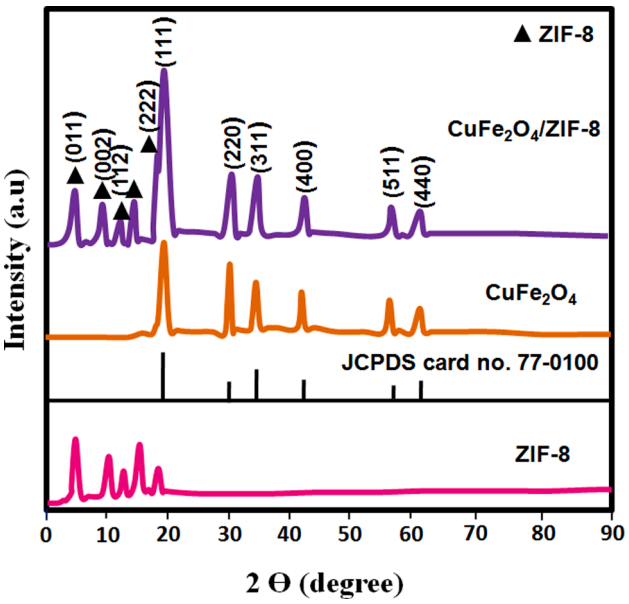

Fig. 1. XRD pattern of the electrode samples.

2.4. Synthesis of $CuFe_2O_4$ and $CuFe_2O_4$/ZIF-8 composite materials

In the synthesis process of $CuFe_2O_4$/ZIF-8, 0.1 g of as-prepared ZIF-8 was stirred in 40 ml of ethanol for 20 min at room temperature. 0.1 mol of Cu-Fe added to precursor solution and stirred for 20 min. The mixed solution was transferred into a 75 ml Teflon container. After sealing, the autoclave was heated to 180 °C for 12 h. The product was collected by centrifugation, washed several times with water and methanol, and vacuum-dried overnight at 70 °C. This final product was named as $CuFe_2O_4$/ZIF-8 composite (light brown in color).

2.5. Characterization techniques:

The crystal structure of prepared electrode samples was determined by the result of X-ray diffraction (XRD, MiniFlex600) using monochromated CuKα radiation. The structure was further investigated by Raman spectra, tested on a Thermo-scientific DXR. The morphology and partixle size of the prepared samples was analyzed by scanning electron microscope (SEM) and a JEOL 2100F high transmission electron microscope (HRTEM). The chemical states of the products were analyzed by a Thermo ESCALAB 250XI X-ray photoelectron spectrometry (XPS). The specific surface area and pore size distribution were tested by a nitrogen adsorption–desorption apparatus (Micromeritics ASAP2020) using the Brunauer–Emmett–Teller (BET) method.

2.6. Electrochemical measurements:

The working electrodes were provided by the mixing active materials (80 wt%), super P (10 wt%), and polyvinylidene fluoride (PVDF) binder (10 wt%) in N-methyl-2-pyrrolidone (NMP) solvent to obtain a slurry. The as-obtained slurry was coated on a copper foil and dried under vacuum. Then, the electrodes were cut into wafers with a diameter of 10 mm. The loading mass of the active materials was kept at about 0.6–0.8 $mgcm^{-2}$. The electrochemical properties were tested with CR2032 coin cells with a lithium metal cathode, a Celgard separator, a $CuFe_2O_4$-based anode, and 1 M LiPF 6 in diethyl carbonate and ethylene carbonate (1:1 in volume) electrolyte. The button batteries were assembled in an argon-filled glovebox. Galvanostatic charge and discharge measurements were

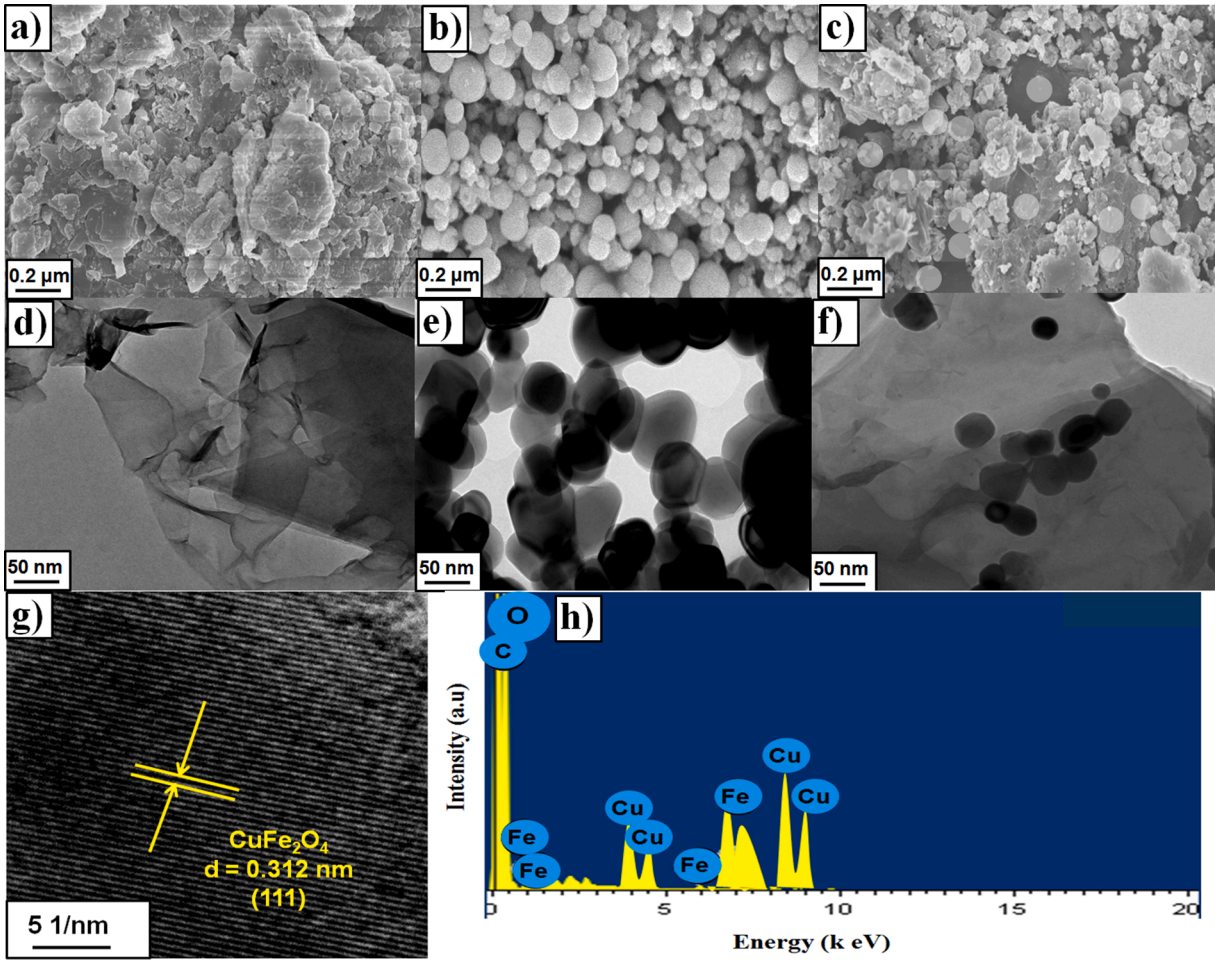

Fig. 2. SEM images of **a)** ZIF-8; **b)** $CuFe_2O_4$; **c)** $CuFe_2O_4$/ZIF-8; TEM images of **d)** ZIF-8; e) $CuFe_2O_4$; **f)** $CuFe_2O_4$/ZIF-8; **g)** HRTEM of $CuFe_2O_4$/ZIF-8; **h)** EDS image of $CuFe_2O_4$/ZIF-8.

conducted on a LAND-CT2001 test system with the voltage ranging between 0.01 and 3.0 V (vs. Li^+ /Li). Cyclic voltammetry (CV) (0.2 mVs^{-1}) and electrochemical impedance spectroscopy (EIS) (100 kHz to 0.01 Hz) were tested using an electrochemical workstation (CHI660D).

3. Results and discussion

3.1. XRD analysis

X-ray diffraction is a truthful characterization technique to understand the structural geographies of ferrite systems. XRD patterns of bare ZIF-8, $CuFe_2O_4$ and $CuFe_2O_4$/ZIF-8 composite samples are displayed in Fig. 1. The XRD pattern of ZIF-8 showed the following miller indices of (011), (002), (112), (022), and (222). All the crystalline plane of perfectly matched with the already reported work [23]. The diffraction patterns of present ferrite systems stood as proof for the formation of the cubic spinel structure. The XRD pattern of pristine $CuFe_2O_4$ had peaks at 18.5°, 30.2°, 35.8°, 43.5°, 57.8°, and 62.6°, which belongs to (111), (220), (311), (400), (511) and (440) planes with cubic structure (JCPDS-77–0100). The diffractions peaks labeled with (111), (220), (311), (400), (511) and (440) are consistent with JCPDS card no. JCPDS-77–0100 and mentioning that the ferrite system belonged to fd3m space group. The diffraction peaks corresponding to the secondary phases of CuO and α-Fe_2O_3 cannot be found from the XRD patterns and demonstrate that prepared sample was highly purity in nature. The lattice parameter, a, was calculated from the diffraction peak using the formula: $a^2 = d^2.(h^2 + k^2 + l^2)$ where d is the inter-reticular distance

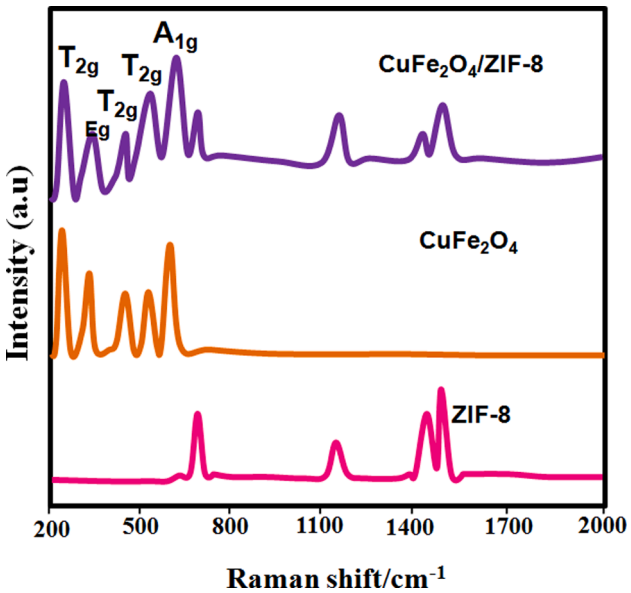

Fig. 3. Raman spectra of the electrode samples.

and hkl are the Miller indices of the plan. For an accurate calculation of the lattice constant, the lattice parameter was calculated for each peak of the XRD pattern and then the average of these values is determined, a =

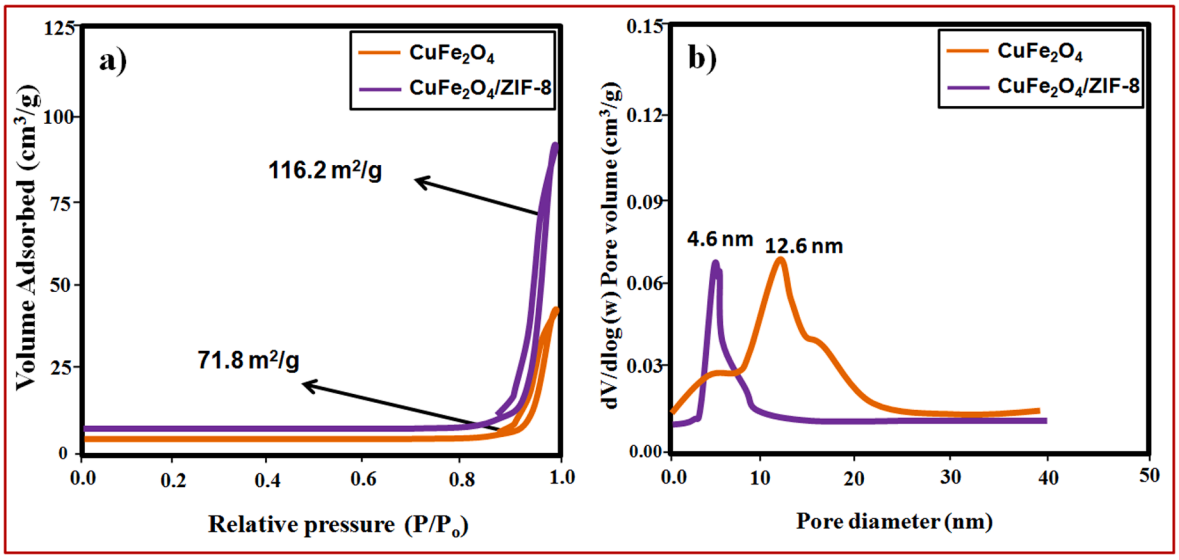

Fig. 4. **a)** N_2 adsorption and desorption analysis of $CuFe_2O_4$ and $CuFe_2O_4$/ZIF-8 electrode samples; **b)** pore size distribution.

(8.376 ± 0.005) Å. In the $CuFe_2O_4$/ZIF-8 composite sample, the ZIF-8 planes [(1 1 1), (0 0 2), (1 1 2), and (2 2 2)] along with $CuFe_2O_4$ can be presented. Hence, the results suggest that successful formation of nanocomposite between $CuFe_2O_4$ and ZIF-8 during the hydrothermal process. Moreover, the diffraction peaks of $CuFe_2O_4$/ZIF-8 composite was become stronger than compared with pristine sample, which suggest that improved crystalline nature. The average grain size of $CuFe_2O_4$ and ZIF-8 was estimated from all the diffraction planes and takes the average values. The estimated grain size is 34.2 ± 0.5 nm and 46.3 ± 0.5 nm for $CuFe_2O_4$ and $CuFe_2O_4$/ZIF-8 composite samples, respectively.

3.2. Morphological analysis

The morphology and particle size of the prepared samples were examined by SEM and TEM studies. Fig. 2 (a-c) shows the SEM images of ZIF-8, $CuFe_2O_4$ and $CuFe_2O_4$/ZIF-8 composite samples, respectively. The SEM image of ZIF-8 is clear nanosheets morphology (Fig. 3a). The smooth and uniform size nanosheet and found with sizes in the range of 250 nm. The smooth outer surface with spherical nanoparticle (20–25

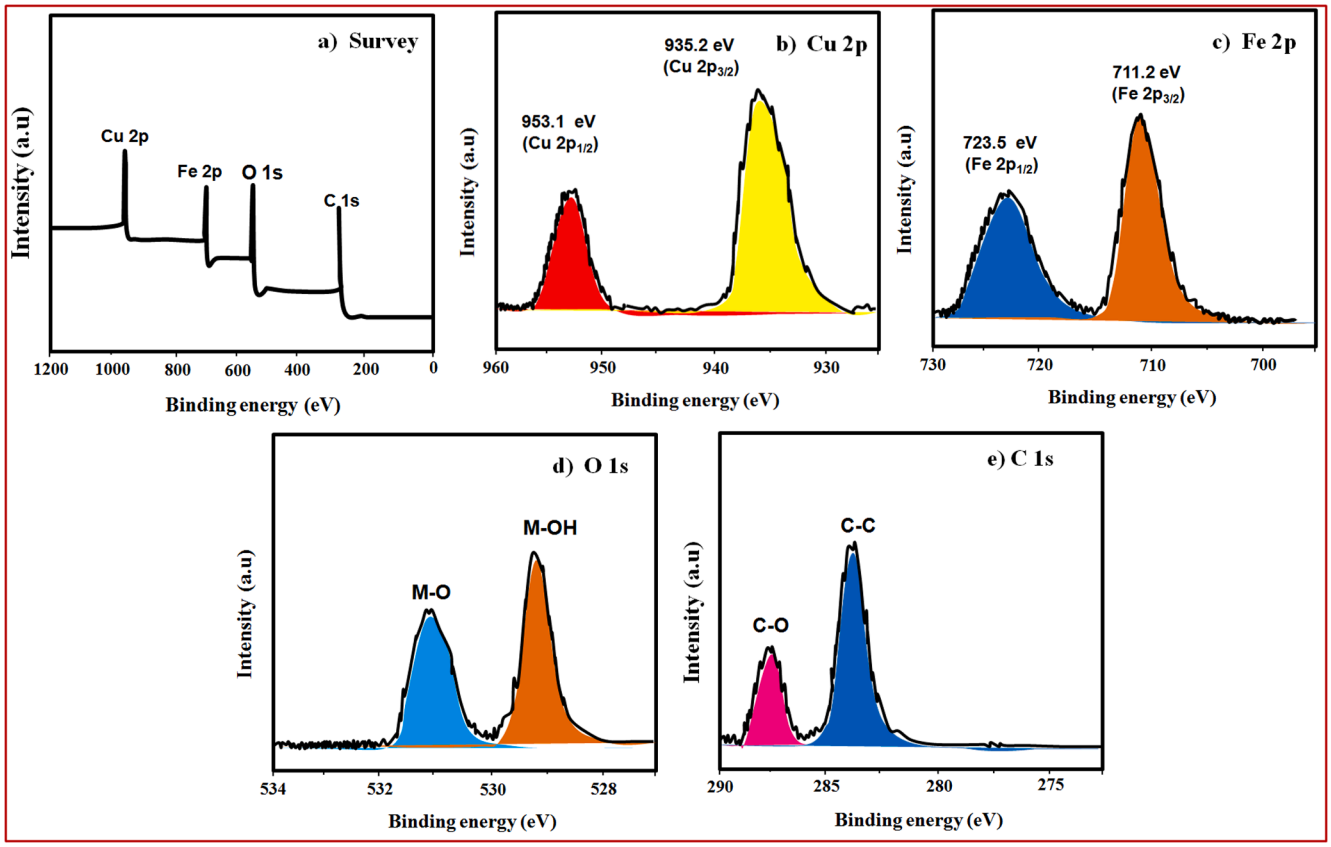

Fig. 5. XPS of $CuFe_2O_4$/ZIF-8 **a)** survey; **b)** Cu 2p; **(c)** Fe 2p; **d)** O 1s and **e)** C 1s.

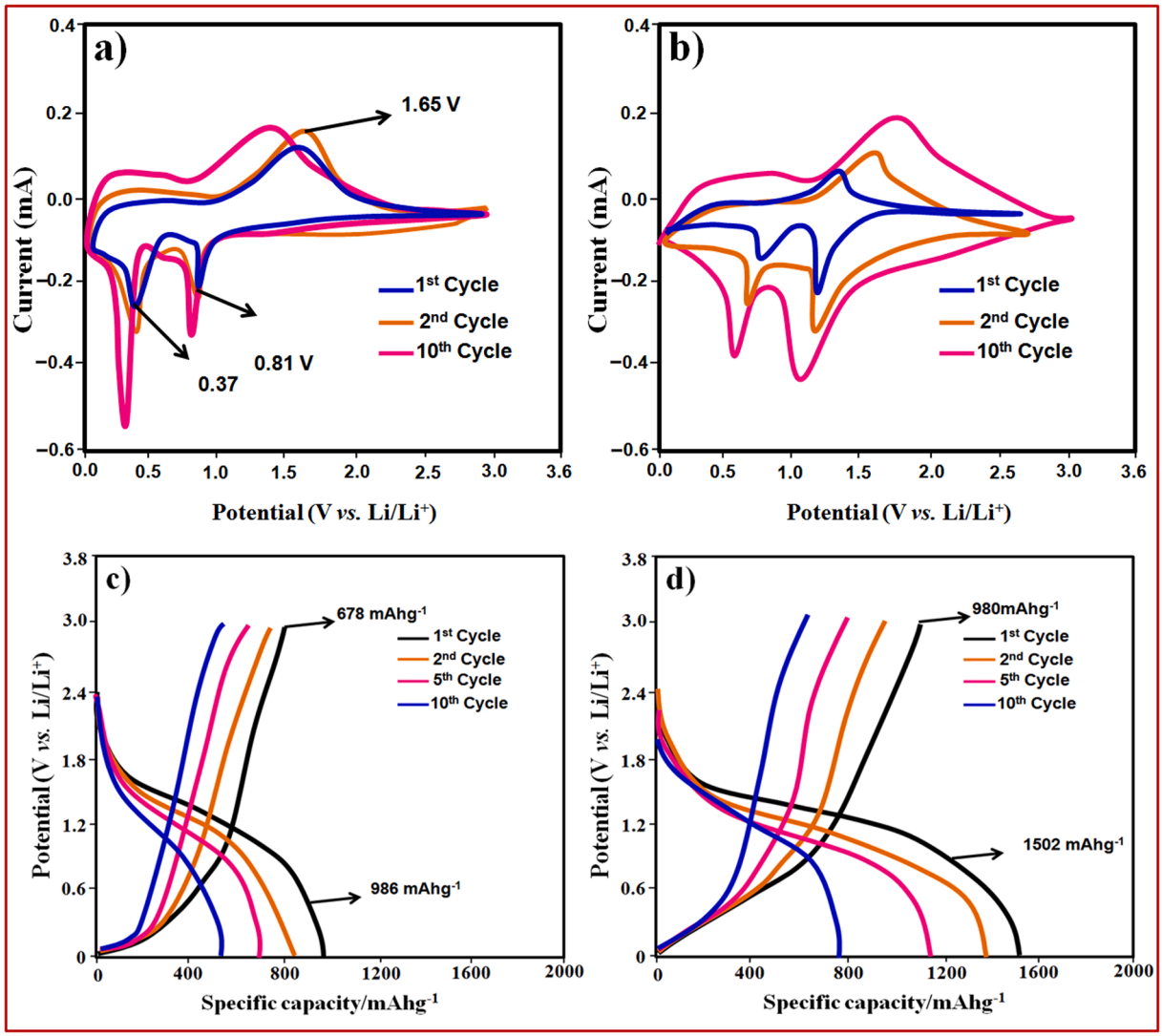

Fig. 6. CV curve of **a)** $CuFe_2O_4$; **b)** $CuFe_2O_4$/ZIF-8 electrodes with various scan rates; Charge-discharge profile of **c)** $CuFe_2O_4$; **d)** $CuFe_2O_4$/ZIF-8.

nm) are uniformly decorated on the surface of ZIF-8 nanosheets (Fig. 3c). The typical ZIF-8 nanosheets and well defined uniform sizes $CuFe_2O_4$ nanoparticles are further confirmed by TEM (Fig. 2d&e). The nanoparticles fully decorated on the surface of ZIF-8 sheets (Fig. 2f). Further the HRTEM image of $CuFe_2O_4$ showed clear lattice fringes values of (0.312 nm). Communicate to the (1 1 1) planes of cubic structure $CuFe_2O_4$. The key elements of Cu, Fe and O are presented in the EDAX image of $CuFe_2O_4$/ZIF-8 (Fig. 2h).

3.3. Raman spectra analysis

The incorporation of ZIF-8 into $CuFe_2O_4$ was further conformed by Raman spectroscopic technique. Fig. 4 shows the room temperature Raman spectra of pure ZIF-8, $CuFe_2O_4$ and $CuFe_2O_4$/ZIF-8 composite samples, respectively. The Raman spectra of ZIF-8 presented at 680, 1142, 1455, 1498 cm is due to the vibration modes of 2-methylimedazole ligand [24]. In pure $CuFe_2O_4$ sample showed five Raman modes for cubic ferrite structure. Namely the A_{1g} mode (711 cm^{-1}) E_g mode (301 cm^{-1}), T_{2g} (482 cm^{-1}), T_{2g} (511 cm^{-1}) and T_{2g} (212 cm^{-1}) [25]. The cubic ferrite structure was also confirmed by XRD results. Both ZIF-8 and $CuFe_2O_4$ Raman modes are existence in the composite samples are also additional support for the nanocomposites between $CuFe_2O_4$ and ZIF-8.

3.4. Textural and surface composition analysis

Generally in the electrochemical behavior pure size and specific area have major impact for the both prepared electrode samples. Hence N_2 absorption –desorption was takes to know their behavior of the prepared electrode samples (Fig. 5). The graph of both isotherms clearly exhibits the type 4 with H3 hysteresis loop which denotes that mesoporous nature of the samples [26–30]. We found that $CuFe_2O_4$/ZIF-8 composite sample derives a high surface area of 116.2 m^2g^{-1} and pore diameter of 4.6 nm, which is higher than that of bare $CuFe_2O_4$/ZIF-8 composite can be reduce the dielectric constant and dielectric resistance. This improves the electro chemical performance of the fabricated device. The surface chemistry and the chemical states of the prepared sample was analyzed by XPS, Fig. 5a shows the wide range survey spectra of $CuFe_2O_4$/ZIF-8. The Cu 2P, Fe 2P, O 1s and C1s spectra is shown in Fig. 5 (b-e). The Cu 2P spectra reveal the two binding energy (BE), which is positioned at 935.2 eV and 952.1 eV is due to Cu $2p_{3/2}$ and Cu $2p_{1/2}$, respectively. The Fe 2p spectra revealed the position of two peaks at 711.2 eV and 723.5 eV which belongs to Fe $2p_{3/2}$ and Fe $2p_{1/2}$ respectively. The high resolution (HR) O1s spectrum was split into two peaks at 531.1 eV and 529.1 eV these peaks are due to M—O and OH group of the absorbed water [31,32]. The C 1s peak can be decomvoluted into two band at 284.1 and 288.2 eV, corresponding to C═C and carboxylate C═O) groups of organic ligand (or) metal organic framework [33].

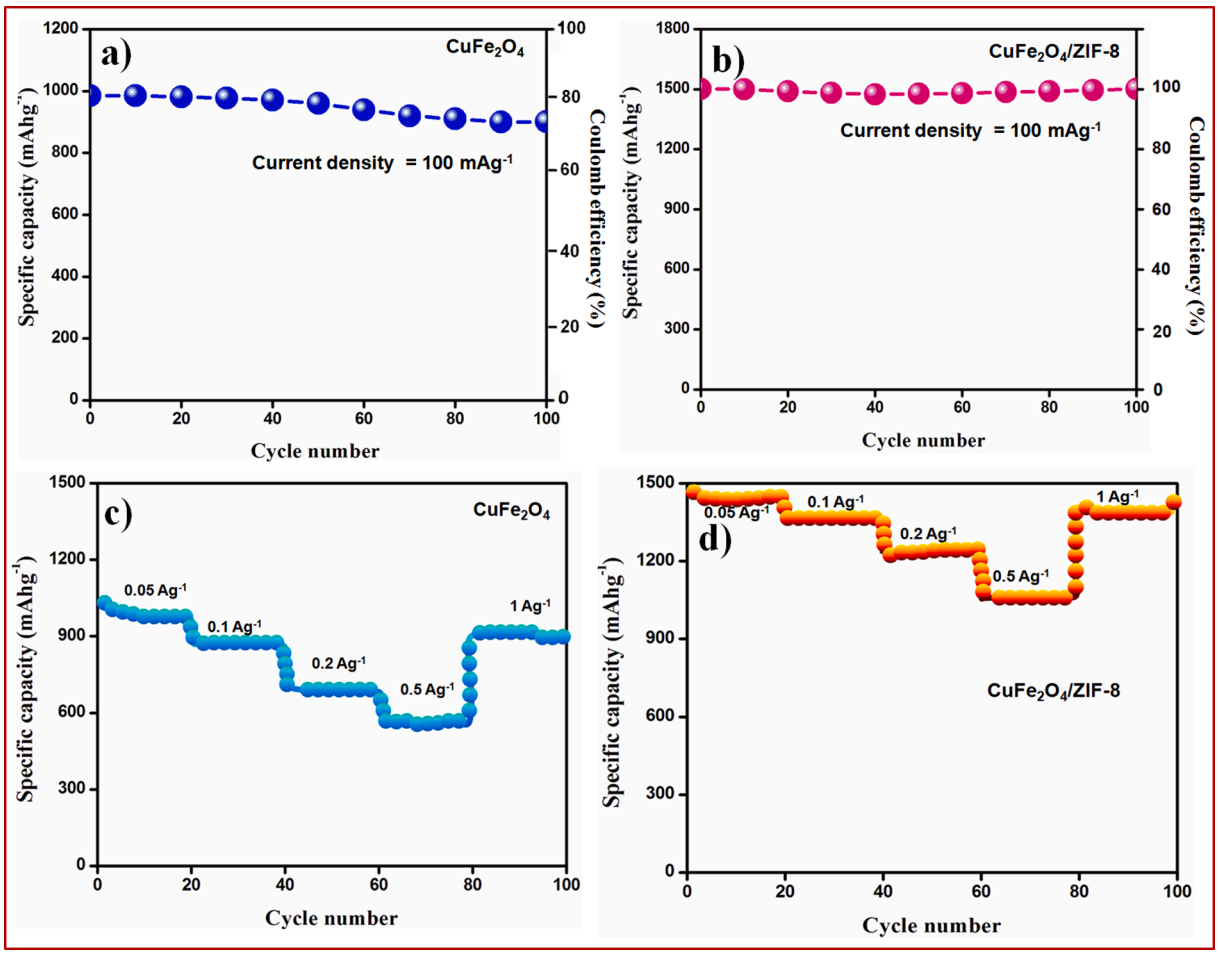

Fig. 7. a) and **b)** Cyclic performance of $CuFe_2O_4$ and $CuFe_2O_4$/ZIF-8 and rare capacity of **c)** $CuFe_2O_4$; **d)** $CuFe_2O_4$/ZIF-8.

3.5. Electrochemical studies

Cyclic voltammetry of both $CuFe_2O_4$ and $CuFe_2O_4$/ZIF-8 electrodes were measured to evaluate the reversibility and electrochemical characteristics behavior. Fig. 6 shows the CV curve of $CuFe_2O_4$ electrode with various cycles (1 to 10) and measured at scan rates of 0.1 mVs^{-1}. Peaks at 1.55 V in the initial cathodic scan can be attributed to the lowering of the irreversible reaction with the medium. In addition, the first cathodic shows two distinct decrease peaks, located at 0.81 V and 0.37 V, correspondingly. The earlier peaks are credited to the reaction process of $CuFe_2O_4$ with Li ion into Cu0 and Fe0 coupled with some further restriction of Cu0 to give a Li-Cu alloy, and the later peaks are credited to the decay of electrolyte to form solid electrolyte interaction (SEI), and the later peaks are credited to the reaction process of $CuFe_2O_4$ with Li ion into Cu0 and Fe0 combined with further restriction of Cu0. The anodic peak at 1.65 V is due to the oxidation of Cu and Fe to CuO and Fe_2O_3. Similar CV curves observed for $CuFe_2O_4$/ZIF-8 electrode indicate the occurrence the same electrochemical reaction (Fig. 6b). The electrochemical reaction mechanism during the first cycle is as given below:

During discharge,

$$CuFe_2O_4 + 8Li^+ + 8e^- \rightarrow Ni + 2Fe + 4Li_2O$$

During charge,

$$Cu + Li_2O \rightarrow CuO + 2Li^+ + 2e\text{-}$$

$$2Fe + 3Li_2O \rightarrow Fe_2O_3 + 6Li+ + 6e^-$$

Overall reaction: $CuFe_2O_4 + 4Li_2O \rightarrow CuO + Fe_2O_3 + 8Li^+ + 8e^-$

From the 2nd cycle onwards, the $CuFe_2O_4$ structure does not exist. Therefore, the reaction mechanism proceeds in the following manner: During discharge,

$$CuO + 2Li^+ + 2e^- \rightarrow Ni + Li_2O$$

$$Fe_2O_3 + 6Li^+ + 6e^- \rightarrow 2Fe + 3Li_2O$$

During charge,

$$Cu + Li_2O \rightarrow CuO + 2Li^+ + 2e^-$$

$$2Fe + 3Li_2O \rightarrow Fe_2O_3 + 6Li+ + 6e^-$$

Fig. 6 (c & d) shows the change-discharge profiles for $CuFe_2O_4$ and $CuFe_2O_4$/ZIF-8 electrodes measured at 100 mAg^{-1} within the potential voltage window of 0.01–3.0 V. In the initial cycle, the discharge /charge capacity of Cu Fe_2O_4/MOF was found to be 1502/980 $mAhg^{-1}$. Similarly the pure $CuFe_2O_4$ electrode exhibits discharge/charge was 986/678 $mAhg^{-1}$. It means that coulomb efficiency of $CuFe_2O_4$/ZIF-8 and $CuFe_2O_4$ was found to be 88 and 67.8 %, respectively. In the end of 10th cycle, the discharge /charge capacity of Cu Fe_2O_4/MOF was found to be 790/695 $mAhg^{-1}$. Similarly the pure $CuFe_2O_4$ electrode exhibits discharge/charge was 560/535 $mAhg^{-1}$. The columbic efficiency of $CuFe_2O_4$/ZIF-8 and $CuFe_2O_4$ was 79 and 69.5%, respectively (10th cycle). The capacity becomes stable with increasing cycles with a coulomb efficiency as high as 97%. Fig. 7 (a) & (b) shows the cyclic performance of pure $CuFe_2O_4$ and $CuFe_2O_4$/ZIF-8 composite electrodes tested at current density of 100 mAg^{-1} for 100 cycles. In pure $CuFe_2O_4$ sample, the reversible capacities rapidly decreases in the initial 50 cycles on centrally the $CuFe_2O_4$/ZIF-8 composite shows excellent reversible

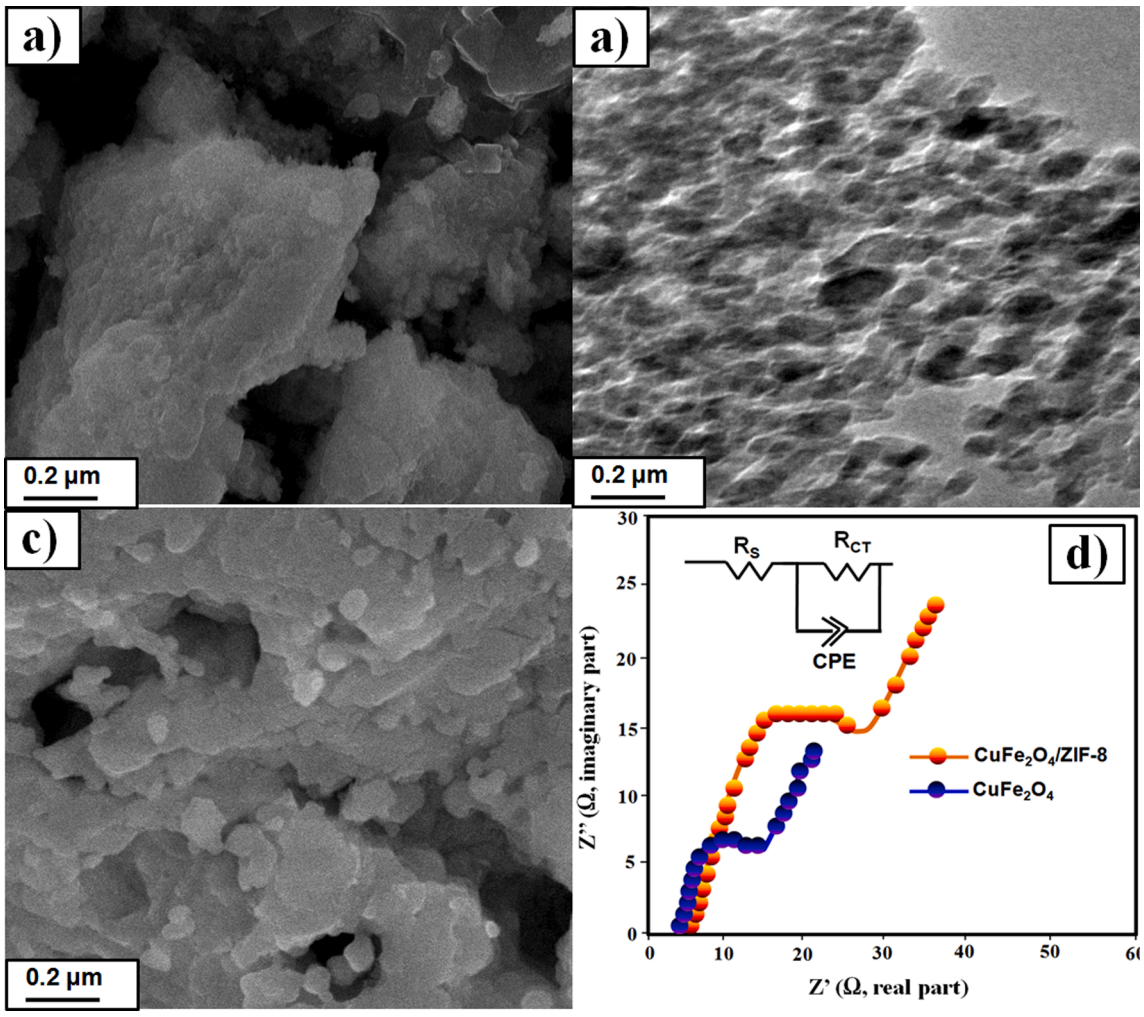

Fig. 8. SEM images of **a)** ZIF-8; **b)** $CuFe_2O_4$; **c)** $CuFe_2O_4$/ZIF-8 composite (after 50 cycling); d) Nyquist plot of $CuFe_2O_4$ and $CuFe_2O_4$/ZIF-8 electrode samples.

capacities stability with maintaining at 1478 $mAhg^{-1}$ until 100 cycles. This enhancement of cycle performance confirms the advantages of binary oxides over single metal oxides as anode materials and the synergistic effect of the synergistic effect between Cu and Fe oxides. Rate capability is another important parameter for LIBs practical application. The rare capacity of the both $CuFe_2O_4$ and $CuFe_2O_4$/ZIF-8 was further evaluated to realize the electrochemical performance of the sample and the relevant plot is shown in the Fig. 7 (c) & (d). The average discharge capacities of $CuFe_2O_4$/ZIF-8 were 1475, 1371, 1201, 991 and 1401 at current densities of 0.05, 0.1, 0.2, 0.5, and 1 Ag^{-1}. Similarly the average discharge capacities of $CuFe_2O_4$ sample were found to be 981, 880, 701, 545 and 975, respectively. Both electrodes can be retained the discharge capacity of about 1401 and 850 mAg^{-1} from 1 to 0.5 Ag^{-1} demonstrating structure stability and favorable reversibility. In order to find out the change of electrode morphology in the cell cycle, we conducted SEM experiment. Fig. 8 (a-c) shows the SEM images of ZIF-8, $CuFe_2O_4$ and $CuFe_2O_4$/ZIF-8 composite samples, respectively. The SEM image of ZIF-8 (Fig. 8a), after 50 cycle is clearly showed that sheet like morphology and the morphology of ZIF-8 was did not change after cycling process. As can be seen from the SEM photograph of the $CuFe_2O_4$ electrode (Fig. 8b), after the 50 cycle, the electrode surface material is evenly distributed, the particle size is uniform, and the electrode structure is complete. The uniform size nanoparticles are evenly decorated on the surface of the ZIF-8 nanosheets (Fig. 8c). To ascertain the reasoning behind the superior performance of the two electrodes, electrochemical impedance spectroscopy was conducted for both pristine and cycled electrodes. The Nyquist plots along with the fitted curves have been shown in 8 (d). As exhibited in Fig. 8d), the EIS spectra composed of a depressed semicircle in the high-frequency region and a sloping line in the low-frequency region. It can be clearly seen that the semicircle with the diameter of the porous $CuFe_2O_4$/ZIF-8 composites is much smaller than that of pure $CuFe_2O_4$. This result shows that the $CuFe_2O_4$/ZIF-8 nanocomposites behave the lower charge transfer resistance between the electrode and electrolyte interface. It can be concluded that the ZIF-8 as efficient charge carrier could facilitate charge transfer at the interface leading to higher rate capability, proving that the $CuFe_2O_4$/ZIF-8 nanocomposites behaves lower charge-transfer and contact impedances as anode for LIBs. From the plot, the initial charge transfer resistance (R_{CT}) values are low and decrease even further after 100 cycles. After 100 cycles, the RCT values for $CuFe_2O_4$ and $CuFe_2O_4$/ZIF-8 electrodes are 15.9 Ω and 7.17 Ω, correspondingly. Low values suggest that the conducting network produced by ZIF-8 and CuFe2O4 facilitates charge transfer, resulting in improved electrocatalytic activity. The overall electrochemical results suggest that ZIF-8 derived $CuFe_2O_4$ electrode showed outstanding results than compared with pure $CuFe_2O_4$. The as-prepared $CuFe_2O_4$/ZIF-8 composite's long-term cycle durability and high-rate performance can be attributed to their well-designed hybrid geometries and compositions, namely mesoporous $CuFe_2O_4$ NPs evenly developing atop conductive ZIF-8 nanosheets. Numerous mesopores within electroactive $CuFe_2O_4$ NPs provide enough electrode–electrolyte interaction area to allow Li + ions to rapidly flux throughout the electrode interface and reduce the Li + ion diffusion range, facilitating better electrochemistry, particularly at high current density [34]. The electrochemical results suggest that $CuFe_2O_4$/

ZIF-8 composite showed better reversible capacity, high retention and long term stability than compared with pristine $CuFe_2O_4$. This could be due to obvious improvement surface area endows $CuFe_2O_4$/ZIF-8 nanocomposites with more contact area between electrolyte and electrode material, and the mesopore structure can facilitate the transportation of electrolyte molecules and Li^+ ions and accommodate the volume variations of the electrode materials during the charge/discharge processes, resulting in enhancement electrochemical properties. Moreover, the mesopores provide more path way for ion transportation and the $CuFe_2O_4$/ZIF-8 composites intertwine to form the porous 2D nanosheets and nanoparticles framework, which could shorten the migration path and enhance the diffusion coefficient of Li^+. Attractive reversible capacities arise from ZIF-8, which could significantly enhance the electrical contact of $CuFe_2O_4$ nanoparticles and limit the $CuFe_2O_4$ expansion only along the axial to facilitate the stress relaxation. Meanwhile, the nanopores among the nanoparticles and the 2D framework are beneficial to improve the electronic conductivity and the diffusion coefficient of Li^+, further improve the rate performance of the electrode.

4. Conclusion

In summary, a new $CuFe_2O_4$/ZIF-8 nanocomposite was designed and prepared via a facile one-pot hydrothermal method. When used as anode for high-performance. LIBs, the $CuFe_2O_4$/ZIF-8 nanocomposites exhibit an excellent electrochemical property in terms of reversible capacity, capacity retentions, and rate capabilities. Attractive reversible capacities arise from ZIF-8, which could significantly enhance the electrical contact of $CuFe_2O_4$ nanoparticles and limit the $CuFe_2O_4$ expansion only along the axial to facilitate the stress relaxation. Meanwhile, the nanopores among the nanoparticles and the 2D framework (ZIF-8 nanosheets) are beneficial to improve the electronic conductivity and the diffusion coefficient of Li^+, further improve the rate performance of the electrode. Such an excellent lithium storage performance demonstrates that the $CuFe_2O_4$/ZIF-8 composites are promising electrode materials for lithium batteries (LIBs).

Declaration of Competing Interest

The authors declare that they have no known competing financial interests or personal relationships that could have appeared to influence the work reported in this paper.

References

[1] P. Pan, L.H. Chen, F. Wang, C.Q. Feng, J. Du, X. Yang, C.Q. Qin, Y. Ding, Cu_2NiSnS_4 nanosphere array on carbon cloth as free-standing and binder-free electrodes for energy storage, Electrochim. Acta 260 (2018) 305–313.

[2] T.-H. Kim, J.-S. Park, S.K. Chang, S. Choi, J.H. Ryu, H.-K. Song, The current move of lithium ion batteries towards the next phase, Adv. Energy Mater. 2 (7) (2012) 860–872.

[3] G. Zhu, Y. Wang, Y. Xia, Ti-based compounds as anode materials for Li-ion batteries, Energy Environ. Sci. 5 (2012) 6652–6667.

[4] F. Cheng, J. Liang, Z. Tao, J. Chen, Functional materials for rechargeable batteries, Adv. Mater. 23 (15) (2011) 1695–1715.

[5] X. Gao, J. Wang, D. Zhang, K. Adair, K. Feng, N.a. Sun, H. Zheng, H. Shao, J. Zhong, Y. Ma, X. Sun, X. Sun, Carbon coated bimetallic sulfide nanodots/carbon nanorod heterostructure enabling long-life lithium-ion batteries, J. Mater. Chem. 5 (48) (2017) 25625–25631.

[6] L. Hou, L. Lian, L. Zhang, G. Pang, C. Yuan, X. Zhang, Self-sacrifice template fabrication of hierarchical mesoporous Bi-component-active ZnO/$ZnFe_2O_4$ sub-microcubes as superior anode towards high-performance lithium-ion battery, Adv. Funct. Mater. 25 (2) (2015) 238–246.

[7] L. Hou, R. Bao, Y. Zhang, X. Sun, J. Zhang, H. Dou, X. Zhang, C. Yuan, Structure designed synthesis of yolk-shell hollow $ZnFe_2O_4$/C@N-doped carbon sub-microspheres as a competitive anode for high-performance Li-ion batteries, J. Mater. Chem. 6 (37) (2018) 17947–17958.

[8] D. Feng, Y. Hui, X. Guo, 3-Dimensional hierarchically porous $ZnFe_2O_4$/C composites with stable performance as anode materials for Li-ion batteries, Chem. Eng. J. 355 (2019) 687–696.

[9] Y. Wang, Y. Lei, J. Li, L.i. Gu, H. Yuan, D. Xiao, Synthesis of 3D-nanonet hollow structured Co_3O_4 for high capacity supercapacitor, ACS Appl. Mater. Interfaces 6 (9) (2014) 6739–6747.

[10] C. Janiak, J.K. Vieth, MOFs, MILs and more: concepts, properties and applications for porous coordination networks (PCNs), New J. Chem. 34 (11) (2010) 2366–2388.

[11] X. Hu, Z. Zhu, F. Cheng, Z. Tao, J. Chen, Micro-nano structured Ni-MOFs as high-performance cathode catalyst for rechargeable Li–O_2 batteries, Nanoscale 7 (28) (2015) 11833–11840.

[12] S.H. Kazemi, Facile synthesis of mixed metal–organic frameworks: electrode materials for supercapacitors with excellent areal capacitance and operational stability, ACS Appl. Mater. Interfaces 10 (27) (2018) 23063–23073.

[13] W. Chaikittisilp, K. Ariga, Y. Yamauchi, A new family of carbon materials: synthesis of MOF-derived nanoporous carbons and their promising applications, J. Mater. Chem. A 1 (1) (2013) 14–19.

[14] H.L. Jiang, From metal–organic framework to nanoporous carbon: toward a very high surface area and hydrogen uptake, J. Am. Chem. Soc. 133 (31) (2011) 11854–11857.

[15] Y. Guo, J. Tang, R.R. Salunkhe, Z.A. Alothman, M.S.A. Hossain, V. Malgras, Y. Yamauchi, Effect of various carbonization temperatures on ZIF-67 derived nanoporous carbons, Bull. Chem. Soc. Jpn. 90 (8) (2017) 939–942.

[16] Y.V. Kaneti, J. Tang, R.R. Salunkhe, X. Jiang, A. Yu, K.-W. Wu, Y. Yamauchi, Nanoarchitectured design of porous materials and nanocomposites from metal-organic frameworks, Adv. Mater. 29 (12) (2017) 1604898.

[17] K. Jayaramulu, Ultrathin hierarchical porous carbon nanosheets for high-performance supercapacitors and redox electrolyte energy storage, Adv. Mater. 30 (2018) 1705789.

[18] H.L. Jiang, T. Akita, T. Ishida, M. Haruta, Q. Xu, Synergistic catalysis of Au@Ag core-shell nanoparticles stabilizedon metal-organic framework, J. Am. Chem. Soc. 133 (2011) 1304–1306.

[19] J. Troyano, A. Carne-Sanchez, C. Avci, I. Imaz, D. Maspoch, Colloidal metal–organic framework particles: the pioneering case of ZIF-8, Chem. Soc. Rev. 48 (2019) 5534–5546.

[20] X.C. Huang, Y.Y. Lin, J.P. Zhang, X.M. Chen, Ligand-directed strategy for zeolite-type metal-organic frameworks: zinc(II) imidazolates with unusual zeolitic topologies, Angew. Chem., Int. Ed. 45 (2006) 1557–1559.

[21] Z. Akimbekov, A.D. Katsenis, G.P. Nagabhushana, G. Ayoub, M. Arhangelskis, A. J. Morris, T. Friščić, A. Navrotsky, Experimental and theoretical evaluation of the stability of true MOF polymorphs explains their mechanochemical interconversions, J. Am. Chem. Soc. 139 (23) (2017) 7952–7957.

[22] S. Tanaka, K. Kida, T. Nagaoka, T. Ota, Y. Miyake, Mechanochemical dry conversion of zinc oxide to zeolitic imidazolate framework, Chem. Commun. 49 (2013) 7884–7886.

[23] Pawan Kumar, Vasudha Bansal, A.K. Paul, Lalit M. Bharadwaj, Akash Deep, Ki-Hyun Kim, Biological applications of zinc imidazole framework through protein encapsulation, Appl. Nanosci. 6 (2016) 951–957.

[24] S. Tanaka, K. Fujita, Y. Miyake, M. Miyamoto, Y. Hasegawa, T. Makino, S. Van der Perre, J. Cousin Saint Remi, T. Van Assche, G.V. Baron, J.F.M. Denayer, Adsorption and diffusion phenomena in crystal size engineered ZIF-8 MOF, J. Phys. Chem. C. 119 (51) (2015) 28430–28439.

[25] R.S. Yadav, J. Havlica, J. Masilko, L. Kalina, J. Wasserbauer, M. Hajdúchová, V. Enev, I. Kuřitka, Z. Kožáková, Cation migration-induced crystal phase transformation in copper ferrite nanoparticles and their magnetic property, J. Supercond. Novel Magn. 29 (3) (2016) 759–769.

[26] S. Sundriyal, V. Shrivastav, H. Kaur, S. Mishra, A. Deep, High-performance symmetrical supercapacitor with a combination of a ZIF-67/rGO composite electrode and a redox additive electrolyte, ACS Omega 3 (12) (2018) 17348–17358.

[27] R. BoopathiRaja, M. Parthibavarman, A. Nishara Begum, Hydrothermal induced novel CuCo2O4 electrode for high performance supercapacitor applications, Vacuum. 165 (2019) 96–104.

[28] R. BoopathiRaja, M. Parthibavarman, Hetero-structure arrays of MnCo2O4 nanoflakes@ nanowires grown on Ni foam: Design, fabrication and applications in electrochemical energy storage, J. Alloys Comp. 811 (2019), 152084.

[29] R. BoopathiRaja, M. Parthibavarman, A. Nishara Begum, Design and fabrication of hierarchical heterostructure $CuCo_2O_4$@PPy based asymmetric device with ultra high capacitance and attractive cycling performance, Mater. Res. Bull. 126 (2020), 110817.

[30] R. BoopathiRaja, M. Parthibavarman, Desert rose like heterostructure of $NiCo_2O_4$/NF@ PPy composite has high stability and excellent electrochemical performance for asymmetric super capacitor application, Electrochimica Acta 346 (2020), 136270.

[31] L. He, W. Zhang, W.u. Hongyuan, Y. Zhao, Zn−Co zeolitic imidazolate framework nanoparticles intercalated in graphene nanosheets for room-temperature NO_2 sensing, ACS Appl. Nano Mater. 4 (2021) 3998–4006.

[32] B. Lesiak, L. Kövér, J. Tóth, J. Zemek, P. Jiricek, A. Kromka, N. Rangam, C sp2/sp3hybridisations in carbon nanomaterials – XPS and (X)AES study, Appl. Surf. Sci. 452 (2018) 223–231.

[33] W. Li, F. Li, H. Yang, X. Wu, P. Zhang, Y.u. Shan, L. Sun, A bio-inspired coordination polymer as outstanding water oxidation catalyst via second coordination sphere engineering, Nat. Commun. 10 (1) (2019).

[34] D. Wang, D. Choi, J. Li, Z. Yang, Z. Nie, R. Kou, D. Hu, C. Wang, L.V. Saraf, J. Zhang, I.A. Aksay, J. Liu, Self-assembled TiO_2-graphene hybrid nanostructures for enhanced Li-Ion insertion, ACS Nano. 3 (4) (2009) 907–914.